Direct Comparison Between Active C-Band Radar and Passive L-Band Radiometer Measurements: Extreme Event Cases

Yili Zhao, Alexis A. Mouche, Bertrand Chapron, and Nicolas Reul

***Abstract*— Co-located over extreme events, C-band co-polarized and cross-polarized normalized radar cross sections (NRCS) and L-band ocean surface roughness brightness temperature ($T_{B,\mathrm{rough}}$) are directly compared to analyze the similarities and differences between these two parameters at medium resolution (about 25 km). NRCS in VH-polarization and VV-polarization ($\sigma_{0,\mathrm{VH}}$, $\sigma_{0,\mathrm{VV}}$) were acquired by Sentinel-1 C-band synthetic aperture radar. $T_{B,\mathrm{rough}}$ is estimated from brightness temperatures (T_B) measured by the L-band radiometer on-board the Soil Moisture Active Passive mission. When the rain rate is less than 20 mm/h, a striking linear relationship is found between active C-Band cross-polarized NRCS and passive L-Band $T_{B,\mathrm{rough}}$: $\sigma_{0,\mathrm{VH}}(\theta_{\mathrm{SAR}}) \propto \tan(\theta_{\mathrm{SAR}}) \times T_{B,\mathrm{rough}}(\theta_{\mathrm{SMAP}} = 40^\circ)$, without any apparent saturation for $T_{B,\mathrm{rough}}$ ranging from 3.5 to 17 K. Compared to both high $T_{B,\mathrm{rough}}$ and $\sigma_{0,\mathrm{VH}}$, co-polarized $\sigma_{0,\mathrm{VV}}$ measurements saturate. As interpreted, this can correspond to a regime change of the air–sea interactions during extreme events. In heavy rain conditions, C-band co-polarized NRCS decreases for extreme situations. In these cases, the covariation between C-band cross-polarized NRCS and L-band $T_{B,\mathrm{rough}}$ is less evident. An accurate and unambiguous assessment of the impact of rain will deserve further investigations.**

***Index Terms*— C-band radar backscatter, L-band emission, tropical cyclone (TC).**

I. Introduction

In RECENT years, new satellite sensor observations have been reported and analyzed to form a more efficient means to probe ocean surfaces under extreme conditions. Hereafter, our main objective is to provide first direct comparisons between these microwave active and passive measurements (on-board two different platforms). As gathered, acquisitions mostly sample extreme conditions, including cases where tropical cyclone (TC) cores were captured. To date, existing studies combining active and passive mostly address low to high wind speeds and rely on airborne data [1], [2].

Foam coverage and thickness conditions resulting from breaking waves are expected to govern the increase in the low-frequency (1.4–7 GHz) microwave emissivity of the ocean surface in storms [3]. A monotone increase in the latter with respect to ocean surface wind speed is now widely used to derive wind fields from radiometer observations over hurricanes [4]–[8]. Recently, Reul *et al.* [9] discussed the remarkable consistency between independent passive measurements from several low-frequency sensors such as the European Space Agency (ESA)/Soil Moisture and Ocean Salinity (SMOS), the National Aeronautics and Space Administration (NASA)/Soil Moisture Active Passive (SMAP), and the JAXA/AMSR-2 to describe the TC size evolution. By contrast, sensitivity differences of contemporaneous C-band co-polarized and cross-polarized radar signals have been recently reported, thanks to new active Synthetic Aperture Radars (SAR) capabilities [10], [11] and airborne measurements [12]. Under extreme conditions, the high sensitivity of cross-polarized normalized radar cross section (NRCS) measurements further help to probe TC winds at very high resolution [13]–[17].

Hereafter, we intentionally disregard the ocean surface wind speed from models or buoys, to take full advantage of precise co-locations (within 60 min) between NRCS acquired in co-polarization and cross-polarization by C-band (5.405 GHz) synthetic aperture radars (C-SARs) on-board ESA's Sentinel-1 missions and the brightness temperatures from SMAP L-band radiometer. This approach prevents any issues regarding the geophysical model function definition, inversion scheme, and reference data quality. Moreover, from sensor physics point of view, rough sea foam and resulting brightness temperature changes can be directly related to the energy flux per unit area [18] and can thus be considered as a direct tracer of the air–sea momentum fluxes.

As reported in [17], the direct analysis of transects in both co-polarized and cross-polarized channels across hurricane eyes (without involving any use of wind measurement) reveal that the cross-polarized signal is four times more sensitive to wind speed than the co-polarized signal. Following this analysis, similarities and differences in active and passive microwave signals induced by the same ocean surface roughness, including extreme weather condition, can thus be analyzed. The data sets and the processing methods are given in Section II. Sections III and IV present the analyses and the conclusions, respectively.

Manuscript received October 3, 2017; revised January 10, 2018; accepted February 7, 2018. This work was supported in part by the National Key Research and Development Program of China under Grant 2016YFC1401001, in part by the National Natural Science Foundation of China under Grant 41501417 and Grant 41406204, in part by the European Space Agency (ESA)/Soil Moisture and Ocean Salinity+STORM evolution through its Support to Science Element Program under Contract CCN2 4000105171/12/I-BG, and in part by ESA SEOM (S1OceanStudy) and Dragon-4 Programs. *(Corresponding author: Yili Zhao.)*

Y. Zhao is with the National Ocean Technology Center, SOA, Tianjin 300112, China, and also with the Laboratoire d'Océanographie Physique Spatiale, 29280 Plouzane, France (e-mail: yzhao@ifremer.fr).

A. A. Mouche is with the Laboratoire d'Océanographie Physique Spatiale, 29280 Plouzane, France, and also with the Nanjing University of Information Science and Technology, Nanjing 210044, China (e-mail: alexis.mouche@ifremer.fr).

B. Chapron and N. Reul are with the Laboratoire d'Océanographie Physique Spatiale, 29280 Plouzane, France.

Color versions of one or more of the figures in this letter are available online at http://ieeexplore.ieee.org.

Digital Object Identifier 10.1109/LGRS.2018.2811712

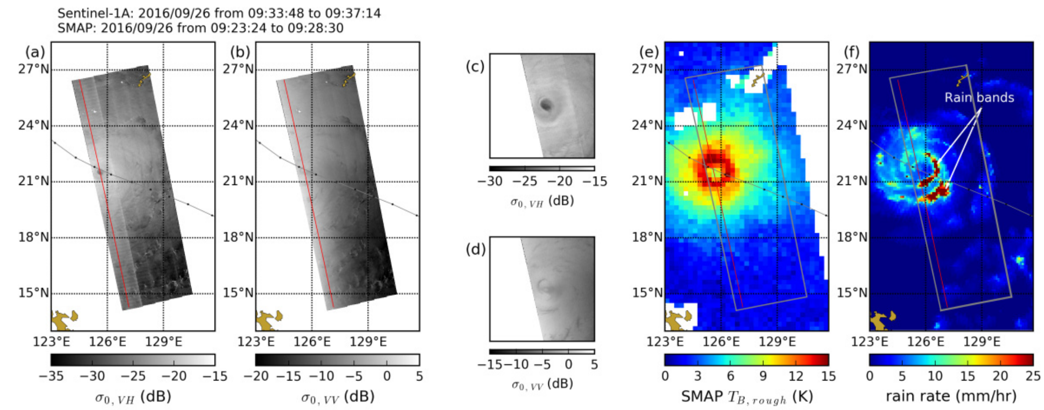

Fig. 1. (a) Images of TC Megi on September 26, 2016. (b) Images of Sentinel-1 $\sigma_{0,\mathrm{VH}}$ and $\sigma_{0,\mathrm{VV}}$. (c) and (d) Enlarged images of $\sigma_{0,\mathrm{VH}}$ and $\sigma_{0,\mathrm{VV}}$ around storm eye. (e) SMAP $T_{B,\mathrm{rough}}$. (f) IMERG rain rate. Red straight lines across storm eye indicate a transect. Gray dotted curves indicate the track of storm.

II. Data Sets and Processing Methodology

A. Sentinel-1 C-Band NRCS

The Sentinel-1 mission is a constellation of two polar-orbiting satellites, Sentinel-1A and Sentinel-1B. They were launched on April 3, 2014 and April 25, 2016, respectively. The C-SARs on-board Sentinel-1 satellites can operate in stripmap (SM), interferometric wide swath (IW), extra-wide swath (EW), and wave mode (WV) exclusive acquisition modes and support measurements in HH + HV-, VV + VH-, HH-, or VV-polarization [19]. The Sentinel-1A and B products in VV + VH-polarization and in IW and EW modes are selected for this letter. They have swaths of 250 and 400 km wide and cover incidence angles from about 18.9° to 47° and from 29.1° to 46.0°, respectively. The spatial resolutions of IW and EW used in this letter are 20×22 m^2 and 93×87 m^2, respectively.

We collected 2222 ESA level-1 ground range detected (GRD) C-SAR products: 1938 (EW 294, IW 1644) products were acquired over north Atlantic between January 1, 2017 and February 22, 2017 and 284 (EW 130, IW 154) products were acquired over TCs in the Northern Hemisphere during the 2016 season.

For Sentinel-1 data processing, thermal noise and GRD border noise are first removed. Then calibration is performed to calculate NRCS (σ_0) [19]. In Fig. 1, four Sentinel-1A acquisitions are combined to capture the full hurricane eye and its associated rain bands. In addition, all the combined products are averaged in a resolution of 500 m. Finally, a land mask is generated to exclude data acquired over land. In this letter, all these preprocessing steps for C-SAR products are completed on Sentinel Application Platform (SNAP) [20].

B. SMAP L-Band $T_{B,rough}$

The L-band radiometer on-board SMAP scans a wide 1000-km swath with a spatial resolution of 40 km. The L-band radiometer measures the four Stokes parameters, T_v, T_h, T_3, and T_4, at a frequency of 1.41 GHz with a surface incidence angle of approximately 40°.

$T_{B,\mathrm{rough}}$ is the quantity used in [4]–[6] and [8] to relate ocean surface L-band emission and ocean surface wind speed. In order to estimate $T_{B,\mathrm{rough}}$ from SMAP antenna measurements, radiometer calibration is applied, and several contributions to the antenna temperature are removed or filtered such as radio frequency interferences, extra-terrestrial contributions (galaxy, sun, etc.), and faraday rotation across the ionosphere [21]. Then atmospheric corrections are performed to estimate brightness temperature emitted by the ocean surface ($T_{B,\mathrm{surface}}$). At last, the brightness temperature of the flat ocean surface, a function of the sea surface salinity (SSS) and sea surface temperature (SST), is subtracted from $T_{B,\mathrm{surface}}$ to get the residual surface roughness-induced brightness temperature: $T_{B,\mathrm{rough}}$. To estimate $T_{B,\mathrm{surface}}$, we used external monthly SSS from World Ocean Atlas (WOA) 2009 and European Center for Medium range Weather Forecasting (ECMWF) 3-h forecast SST.

SMAP L-band radiometer can measure the same target from two different azimuth angles, thanks to the rotating scan of the antenna. $T_{Bh,\mathrm{rough}}$ and $T_{Bv,\mathrm{rough}}$ measured forward and afterward of the SMAP position are averaged to reduce directional variation. In this letter, we consider the first Stokes parameter $(T_{Bh,\mathrm{rough}}+T_{Bv,\mathrm{rough}})/2.0$ for analysis against Sentinel-1 NRCS. The spatial resolution of original NASA level 1B SMAP data is about 40 km, but the reprocessed SMAP product used in this letter is mapped onto a global grid with spatial resolution of 0.25°, and the ascending and descending pass data are saved in independent grids.

C. IMERG Rain Rate

We also rely on Integrated Multisatellite Retrievals for Global Precipitation Measurement (IMERG) products for rain rate. They are generated by intercalibrating, merging, and interpolating estimates from satellite microwave sensors (e.g., GMI, AMSR2, and MHS) together with estimates from microwave-calibrated infrared (IR) sensors on-board Meteosat prime series, GOES-E series, Himawari series, precipitation gauge analyses, and potentially other precipitation estimators at fine time and space scales over the entire globe [22]. These IMERG products are mapped onto a global 0.1° grid with a temporal resolution of half-an-hour. As evaluated in [23], an root mean square of half-hourly rain rate of real-time products is about 3 mm. In this letter, IMERG late product in version 4 is used.

D. Co-Location

To perform accurate analysis of Sentinel-1 NRCS and SMAP $T_{B,\mathrm{rough}}$, we co-locate SMAP $T_{B,\mathrm{rough}}$ with Sentinel-1

This article has been accepted for inclusion in a future issue of this journal. Content is final as presented, with the exception of pagination.

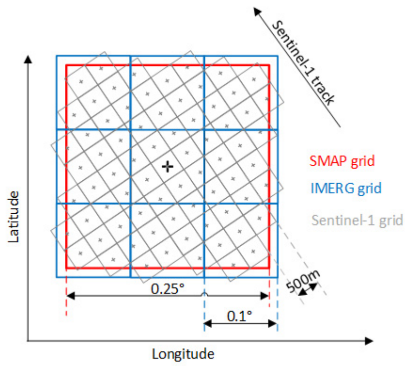

Fig. 2. Sketch for illustrating the co-location of Sentinel-1 NRCS, SMAP $T_{B,\mathrm{rough}}$, and IMERG rain rate.

NRCS, and IMERG rain rate as illustrated in Fig. 2. For spatial co-location, the Sentinel-1 NRCS pixels located in the same SMAP grid are arithmetically averaged (in linear scale) to obtain a match up with SMAP $T_{B,\mathrm{rough}}$ on the very same grid. Considering the spatial resolution of preprocessed Sentinel-1 NRCS and SMAP grid size, pixel of SMAP grid can contain up to 2500 Sentinel-1 valid pixels. The grids with less than 1300 valid Sentinel-1 pixels are excluded. The same processing is applied to IMERG rain rate data. For temporal co-location, the time difference between Sentinel-1 sensing and SMAP measuring is constrained to be less than 60 min, and IMERG data is interpolated at SMAP measuring time. Sentinel-1 A and B have a local time of the ascending node (LTAN) at 6:00 P.M. with a repeat cycle of 12 days and SMAP has the same LTAN with a repeat cycle of 8 days, which increases the possibility of co-location. Finally, we found 975 (EW 210, IW 765) Sentinel-1 products colocalized with SMAP data.

III. Analysis of NRCS and $T_{B,\mathrm{rough}}$

A. Case Analysis

Fig. 1 presents acquisitions of the different types of data used in this letter for the particular case of Typhoon Megi on September 26, 2016 at about 9:30 Universal Time Coordinated (UTC). At this time, intensity of Megi from the best track data indicates Category 2 on the Saffir–Simpson scale with a maximum 1-min sustained surface wind speed of 95 and 90 kt, at 6:00 UTC and 12:00 UTC, respectively. The storm eye is clearly observed in SMAP $T_{B,\mathrm{rough}}$ and Sentinel-1 NRCS in VH-polarization ($\sigma_{0,\mathrm{VH}}$) and is surrounded by a ring of brighter signal showing a maximum at about 50 km from the storm center. Here, the storm center defined by the minimum of SMAP $T_{B,\mathrm{rough}}$ is located at 21.6°N, 125.7°E. The shape of the eye is less obvious in the co-polarized NRCS ($\sigma_{0,\mathrm{VV}}$) signal. This is in line with the reported sensitivity of the co-polarized and cross-polarized NRCS across storm eye as analyzed in [17]. At SMAP and Sentinel-1 acquisition times, IMERG rain rate reaches maximum values around 50 mm/h found in two spiraling bands of heavy rain on the southeast of the storm center (see annotations in Fig. 1).

A transect (red line) across the storm eye and the two rain bands is selected at a fixed incidence angle for Sentinel-1.

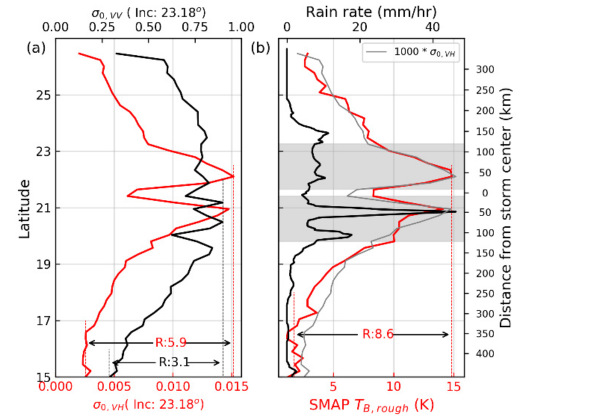

Fig. 3. Analysis along transect across TC eye. (a) Sentinel-1 $\sigma_{0,\mathrm{VH}}$ and $\sigma_{0,\mathrm{VV}}$ at spatial resolutions of 25 km at different latitudes, red line and black line represent $\sigma_{0,\mathrm{VH}}$ and $\sigma_{0,\mathrm{VV}}$, respectively. (b) SMAP $T_{B,\mathrm{rough}}$ and IMERG rain rate at different latitudes, red line and black line represent $T_{B,\mathrm{rough}}$ and rain rate, respectively. R gives the ratio of the values indicated by arrows.

As such, effects due to incidence angle variation or noise fluctuation across the swath are removed. As shown in Fig. 3, when compared at the same spatial resolution, $\sigma_{0,\mathrm{VH}}$ and SMAP $T_{B,\mathrm{rough}}$ display similar increase from the outer storm eye to the storm eye wall. The signal structures around the storm eye are also very consistent in both active and passive measurements. The magnitude between the outer storm signal values at 16.0°N and at 22.0°N (where the maxima are detected) is about six for $\sigma_{0,\mathrm{VH}}$ and nine for $T_{B,\mathrm{rough}}$. A factor of about 1000 is found between $\sigma_{0,\mathrm{VH}}$ and SMAP $T_{B,\mathrm{rough}}$. Indeed, when taking into account this factor [see Fig. 3(b)], C-band $\sigma_{0,\mathrm{VH}}$ and L-band $T_{B,\mathrm{rough}}$ profiles across Megi hurricane are almost identical. In contrast to $\sigma_{0,\mathrm{VH}}$, $\sigma_{0,\mathrm{VV}}$ clearly saturates between 19°N and 24°N close to the storm eye. For this transect, the magnitude of $\sigma_{0,\mathrm{VV}}$ between lowest and highest values is about three.

For this particular TC case, the two major rain bands as detected in IMERG product are about 25 km wide. The band closest to the storm eye has a maximum rain rate of about 40 mm/h at 25-km resolution and is crossed by the selected transect at 20.9°N. The second band has a rain rate of about 20 mm/h and is located at 20°N, about 100 km from the storm center where the hurricane wind speed is expected to decrease. It is difficult to precisely quantify the rain impact on both C-band $\sigma_{0,\mathrm{VH}}$ and L-band $T_{B,\mathrm{rough}}$ from a single example. The performances of the merged IMERG rain measurements product in the specific case of hurricanes are also uncertain. To compute the L-band $T_{B,\mathrm{rough}}$, the contributions of the SST and SSS to the signal are removed. In such an extreme case, intense rain conditions may significantly affect SST and SSS and results in brightness temperature modifications. As a matter of fact, we observe that the linear relationship between L-band $T_{B,\mathrm{rough}}$ and C-band $\sigma_{0,\mathrm{VH}}$ is not anymore valid in the southern part of the eye where much more intense rain is observed than that in the northern part of the eye. When comparing the southern and northern areas of the transect [see gray areas in Fig. 3(b) on each side of the eye], it can be seen that the two signal profiles are quite different near the peaks. This is particularly true for the L-band $T_{B,\mathrm{rough}}$.

This article has been accepted for inclusion in a future issue of this journal. Content is final as presented, with the exception of pagination.

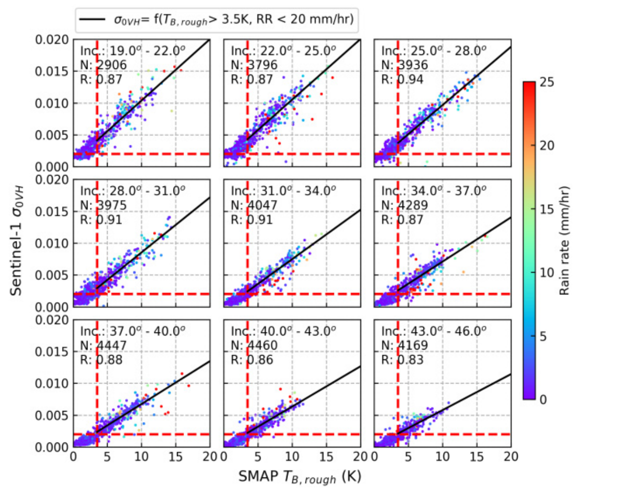

Fig. 4. Sentinel-1 $\sigma_{0,\mathrm{VH}}$ versus SMAP $T_{B,\mathrm{rough}}$ for difference incidence angle and rain rate. Inc., *N*, and *R* are incidence angle, the number of points, and the Pearson correlation coefficient, respectively.

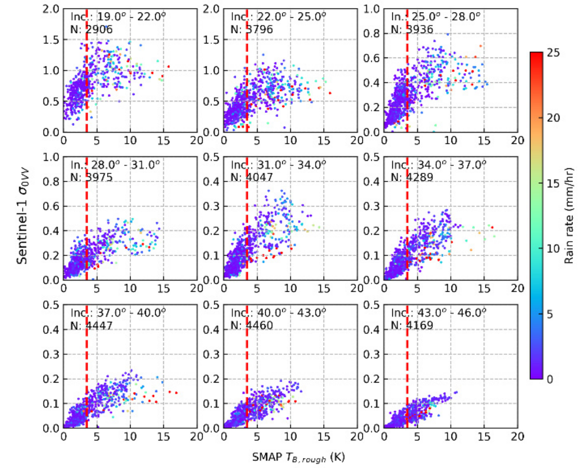

Fig. 5. Sentinel-1 $\sigma_{0,\mathrm{VV}}$ versus SMAP $T_{B,\mathrm{rough}}$ for different incidence angle and rain rate. Inc. and *N* are incidence angle and the number of points, respectively.

A broader shape is found near the location of the second rain band, whereas a narrower shape is found near the location of the first and more intense rain band. For C-band $\sigma_{0,\mathrm{VH}}$, we observe very similar shapes between northern and southern parts of the transects. In this case, where NRCS has been spatially averaged at 25-km resolution, this tends to indicate a small impact of heavy rain on C-band $\sigma_{0,\mathrm{VH}}$ when wind speed is more intense (here we are close to the eye). We also note fluctuations in the NRCS near the location of the second and weaker rain band where wind is expected to be lower (here it is far from eye). This may indicate a possible increase of C-band $\sigma_{0,\mathrm{VH}}$ due to rain when wind decreases. Contrary to the $\sigma_{0,\mathrm{VH}}$ profile, the $\sigma_{0,\mathrm{VV}}$ one's exhibits a significant decrease (by a factor of 50%) coincidently with the two rain bands.

B. Statistical Analysis

Analyses in [6] and [8] both show that $T_{B,\mathrm{rough}}$ in horizontal ($T_{Bh,\mathrm{rough}}$) and vertical ($T_{Bv,\mathrm{rough}}$) polarizations start to linearly increase with ocean surface wind speed for values greater than 11 m/s [8]. For a wind speed of 11 m/s, $T_{Bh,\mathrm{rough}}$ is about 4.5 K and $T_{Bv,\mathrm{rough}}$ is about 2.1 K. Here, we use a reference value of 3.5 K as the lowest $T_{B,\mathrm{rough}}$ value for our analysis.

A threshold of 0.002 is also applied to exclude Sentinel-1 $\sigma_{0,\mathrm{VH}}$ lower than noise equivalent sigma zero (NESZ) where signal-to-noise ratio (SNR) can be weak. The threshold is an approximation of the top NESZ value presented in [11] for Sentinel-1 EW mode in cross-polarization. Note that we only use Sentinel-1 NRCS acquired in the EW mode for analyses (i.e., results shown in Figs. 4 and 5).

Sentinel-1 EW mode covers incidence angles ranging from 18.9° to 47.0°. We, therefore, split the co-locations into nine different incidence-angle range groups with bin width of 3°. In Fig. 4, we present for each of these nine incidence angle bins the SMAP L-band $T_{B,\mathrm{rough}}$ (x-axis in Kelvin) against Sentinel-1 C-band $\sigma_{0,\mathrm{VH}}$ (y-axis in linear unit). The color code indicates the rain rate (in millimeter per hour). For rain rate lower than 20 mm/h, C-band $\sigma_{0,\mathrm{VH}}$ (linear value) linearly increases with SMAP $T_{B,\mathrm{rough}}$ at all incidence angles. This linear trend sustains up to about 17 K for all SAR incidence angles between 19° and 40° and up to 12 K for larger incidence angles. No saturation is observed in the C-band $\sigma_{0,\mathrm{VH}}$. The linear relationship is incidence angle-dependent and may be expressed as

$$\sigma_{0,\mathrm{VH}}(\theta_{\mathrm{SAR}}) = K(\theta_{\mathrm{SAR}}) \times T_{B,\mathrm{rough}}(\theta_{\mathrm{SMAP}} = 40°)$$

where $K(\theta_{\mathrm{SAR}}) = 1.24\mathrm{e}^{-3}–7.06\mathrm{e}^{-4} \times \tan(\theta_{\mathrm{SAR}})$, valid for θ_{SAR} in the range between 19° and 46°. For heavy rain conditions (RR > 20 mm/h), this linear relationship is not clear anymore. This indicates that L-band $T_{B,\mathrm{rough}}$ and C-band $\sigma_{0,\mathrm{VH}}$ do not have the same sensitivity to rain- or induced rain effects (e.g., SSS changes) when computed at 25-km resolution.

The scattering plots of Sentinel-1 $\sigma_{0,\mathrm{VV}}$ against SMAP $T_{B,\mathrm{rough}}$ are shown in Fig. 5. $\sigma_{0,\mathrm{VV}}$ increases with $T_{B,\mathrm{rough}}$ for incidence angles ranging from 19.0° to 34° until $T_{B,\mathrm{rough}} =$ 7.5 K. Then $\sigma_{0,\mathrm{VV}}$ starts to decline. For incidence angles between 34° and 40°, these two regimes in the $\sigma_{0,\mathrm{VV}}$ variation with respect to $T_{B,\mathrm{rough}}$ are still observed but exhibit less spread. $\sigma_{0,\mathrm{VV}}$ dynamic is found to be smaller at large incidence angles with maximum lower than 0.3 (−5.23 dB). The coanalysis between C-band $\sigma_{0,\mathrm{VV}}$ and L-band $T_{B,\mathrm{rough}}$ indicates a loss of sensitivity of $\sigma_{0,\mathrm{VV}}$ for $T_{B,\mathrm{rough}} >$ 7.5 K. A larger scatter between $T_{B,\mathrm{rough}}$ and $\sigma_{0,\mathrm{VV}}$ behavior than between $T_{B,\mathrm{rough}}$ and $\sigma_{0,\mathrm{VH}}$ behavior is also observed. We attribute this larger scatter to the wind direction effect on $\sigma_{0,\mathrm{VV}}$, which is larger than the effect for $\sigma_{0,\mathrm{VH}}$ [10], [13]. In addition, the analysis presented in Fig. 5 suggests that the rain tends to diminish the $\sigma_{0,\mathrm{VV}}$ values at all incidence angles.

IV. Conclusion

In this letter, we directly compared co-located C-band cross- ($\sigma_{0,\mathrm{VH}}$) and co-polarized ($\sigma_{0,\mathrm{VV}}$) NRCS values observed by Sentinel-1 (for incidence angles ranging from 19.0° to 46.0°) with $T_{B,\mathrm{rough}}$ measured by SMAP (at 40° incident angle) in TCs.

Our analyses show that the C-band cross-polarized backscattered signal has a sensitivity very similar to L-band passive sensors. For a given incidence angle, a proportional factor can be found between both quantities and we propose a simple analytical formula to relate them. Contrarily, the C-band $\sigma_{0,\mathrm{VV}}$ sensitivity generally decreases for $T_{B,\mathrm{rough}}$ values larger than 7.5 K. In terms of wind speed, based on the relationship from [8], the linear relationships between C-band $\sigma_{0,\mathrm{VH}}$ and L-band $T_{B,\mathrm{rough}}$ remains valid for wind speeds up to 50 m/s, and C-Band $\sigma_{0,\mathrm{VV}}$ seems to lose its sensitivity for wind speeds larger than 20–30 m/s (depending on the incidence angle).

Although co-polarized and cross-polarized C-band NRCS were reported to be strongly sensitive to wave breaking processes (see [24]) for light to moderate winds, there is an apparent contradiction in the sensitivity between co-polarized and cross-polarized channels. Yet, under extreme conditions, the increased transfer of energy per unit area can result in direct disruption of the interface between air and water, through the development of Kelvin–Helmholtz (KH) instabilities [25]. As such, long breaking waves may be less impacted than shorter wave breakers that can be totally wiped out. Such a physical mechanism may explain the differing sensitivity between the overall microwave emissivity and co-polarized backscatter signals. Using dual-polarized SAR measurements, this differing sensitivity will also be traced in co-polarized and cross-polarized signals, to open improved ways to characterize the air–sea momentum fluxes under extreme conditions at very high resolution (~500 m).

From a more applicative point of view, this letter confirms that having both co-polarization and cross-polarization channels on the future generation of scatterometers such as the next MeTop-SG will be a strong asset for wind measurements over extreme conditions [17]. Moreover, in the view of producing long-term series of homogeneous wind measurements from multiple sources, we anticipate that the use of this new channel should reduce the inconsistencies between L-band radiometers winds and C-band scatterometers winds pointed out in [26].

At 25-km resolution, when the rain rate is significant (>20 mm/h), we found that the sensitivities of L-band $T_{B,\mathrm{rough}}$ and C-band $\sigma_{0,\mathrm{VH}}$ are different. Uncertainties in the computation of the flat ocean surface contribution and in the rain rate over extreme events such as hurricanes make the error analysis quite challenging. A thorough assessment of the rain impact on both sensors certainly deserves further specific studies.

ACKNOWLEDGMENT

The authors would like to thank J. Tenerelli (Ocean Data Lab, France) for providing the gridded SMAP data. Y. Zhao would like to thank the China Scholarship Council for supporting this letter in LOPS-Laboratoire d'Océanographie Physique et Spatiale/Institut Francais de Recherche pour l'Exploitation de la Mer of France.

REFERENCES

[1] Y. G. Trokhimovski and V. G. Irisov, "The analysis of wind exponents retrieved from microwave radar and radiometric measurements," *IEEE Trans. Geosci. Remote Sens.*, vol. 38, no. 1, pp. 470–479, Jan. 2000.

[2] W. J. Plant and V. Irisov, "A joint active/passive physical model of sea surface microwave signatures," *J. Geophys. Res. Oceans*, vol. 122, no. 4, pp. 3219–3239, Apr. 2017.

[3] N. Reul and B. Chapron, "A model of sea-foam thickness distribution for passive microwave remote sensing applications," *J. Geophys. Res. Oceans*, vol. 108, no. C10, p. 3321, Oct. 2003.

[4] N. Reul *et al.*, "SMOS satellite L-band radiometer: A new capability for ocean surface remote sensing in hurricanes," *J. Geophys. Res. Oceans*, vol. 117, no. C02006, Feb. 2012.

[5] N. Reul *et al.*, "A revised L-band radio-brightness sensitivity to extreme winds under tropical cyclones: The five year SMOS-storm database," *Remote Sens. Environ.*, vol. 180, pp. 274–291, Jul. 2016.

[6] S. H. Yueh *et al.*, "SMAP L-band passive microwave observations of ocean surface wind during severe storms," *IEEE Trans. Geosci. Remote Sens.*, vol. 54, no. 12, pp. 7339–7350, Dec. 2016.

[7] E. V. Zabolotskikh, N. Reul, and B. Chapron, "Geophysical model function for the AMSR2 C-band wind excess emissivity at high winds," *IEEE Geosci. Remote Sens. Lett.*, vol. 13, no. 1, pp. 78–81, Jan. 2016.

[8] T. Meissner, L. Ricciardulli, and F. J. Wentz, "Capability of the SMAP mission to measure ocean surface winds in storms," *Bull. Amer. Meterol. Soc.*, vol. 98, no. 8, pp. 1660–1677, Aug. 2017.

[9] N. Reul *et al.*, "A new generation of tropical cyclone size measurements from space," *Bull. Amer. Meterol. Soc.*, vol. 98, no. 11, pp. 2367–2385, Nov. 2017.

[10] P. W. Vachon and J. Wolfe, "C-band cross-polarization wind speed retrieval," *IEEE Geosci. Remote Sens. Lett.*, vol. 8, no. 3, pp. 456–459, May 2011.

[11] A. Mouche and B. Chapron, "Global C-band Envisat, RADARSAT-2 and Sentinel-1 SAR measurements in copolarization and cross-polarization," *J. Geophys. Res. Oceans*, vol. 120, no. 11, pp. 7195–7207, Nov. 2015.

[12] J. W. Sapp, S. O. Alsweiss, Z. Jelenak, P. S. Chang, S. J. Frasier, and J. Carswell, "Airborne co-polarization and cross-polarization observations of the ocean-surface NRCS at C-band," *IEEE Trans. Geosci. Remote Sens.*, vol. 54, no. 10, pp. 5975–5992, Oct. 2016.

[13] B. Zhang and W. Perrie, "Cross-polarized synthetic aperture radar: A new potential measurement technique for hurricanes," *Bull. Amer. Meterol. Soc.*, vol. 93, no. 4, pp. 531–541, Apr. 2012.

[14] G.-J. van Zadelhoff *et al.*, "Retrieving hurricane wind speeds using cross-polarization C-band measurements," *Atmos. Meas. Technol.*, vol. 7, no. 2, pp. 437–449, Feb. 2014.

[15] J. Horstmann, S. Falchetti, C. Wackerman, S. Maresca, M. J. Caruso, and H. C. Graber, "Tropical cyclone winds retrieved from C-band cross-polarized synthetic aperture radar," *IEEE Trans. Geosci. Remote Sens.*, vol. 53, no. 5, pp. 2887–2898, May 2015.

[16] P. A. Hwang, W. Perrie, and B. Zhang, "Cross-polarization radar backscattering from the ocean surface and its dependence on wind velocity," *IEEE Geosci. Remote Sens. Lett.*, vol. 11, no. 12, pp. 2188–2192, Dec. 2014.

[17] A. A. Mouche, B. Chapron, B. Zhang, and R. Husson, "Combined co- and cross-polarized SAR measurements under extreme wind conditions," *IEEE Trans. Geosci. Remote Sens.*, vol. 55, no. 12, pp. 6746–6755, Dec. 2017.

[18] A. C. Newell and V. E. Zakharov, "Rough sea foam," *Phys. Rev. Lett.*, vol. 69, no. 8, pp. 1149–1151, Aug. 1992.

[19] R. Piantanida, G. Hajduch, and J. Poullaouec, "Sentinel-1 level 1 detailed algorithm definition (MPC-0307)," S1-MPC, Tech. Rep. SEN-TN-52-7445, 2017.

[20] ESA. *ESA/STEP*. Accessed: Mar. 14, 2018. [Online]. Available: http://step.esa.int/main/toolboxes/snap

[21] J. Piepmeier *et al.*, "Algorithm theoretical basis document SMAP L1B radiometer brightness temperature data product: L1B_TB," NASA/GSFC, Greenbelt, MD, USA, Tech. Rep. SMAP-ALGMS-RPT-0026, 2016.

[22] G. J. Huffman *et al.*, *NASA Global Precipitation Measurement (GPM) Integrated Multi-Satellite Retrievals for GPM (IMERG)*, Algorithm Theoretical Basis Document (ATBD) V4.5, NASA/GSFC, Greenbelt, MD, USA, 2014.

[23] O. Sungmin *et al.*, "Evaluation of GPM IMERG Early, Late, and Final rainfall estimates using WegenerNet gauge data in southeastern Austria," *Hydrol. Earth Syst. Sci.*, vol. 21, no. 12, pp. 6559–6572, Dec. 2017.

[24] V. Kudryavtsev, I. Kozlov, B. Chapron, and J. A. Johannessen, "Quad-polarization SAR features of ocean currents," *J. Geophys. Res. Oceans*, vol. 119, no. 9, pp. 6046–6065, Sep. 2014.

[25] A. Soloviev and R. Lukas, *The Near-Surface Layer of the Ocean: Structure, Dynamics and Applications* (Atmospheric and Oceanographic Sciences Library), vol. 31. Dordrecht, The Netherlands: Springer, 2006.

[26] L. Pineau-Guillou *et al.*, "Strong winds in a coupled wave-atmosphere model during a North Atlantic storm event: evaluation against observations," *Quart. J. Roy. Meteorol. Soc.*, to be published, doi: 10.1002/qj.3205.